Research on Microstructure, Mechanical and Tribological Properties of Cr-Ti-B-N Films

Lihua Yu *, Huang Luo, Jianguo Bian, Hongbo Ju and Junhua Xu

School of Materials Science and Engineering, Jiangsu University of Science and Technology, Mengxi Road 2, Zhenjiang 212003, China; daniferlh@163.com (H.L.); joycexql@163.com (J.B.); hbju@rocketmail.com (H.J.); jhxu@just.edu.cn (J.X.)

* Correspondence: lhyu6@just.edu.cn; Tel.: +86-150-5111-9966

Abstract: In this study, the Cr-Ti-B-N composite thin films with different Ti and B contents in the films were fabricated by a reactive magnetron sputtering system using chromium (Cr) and TiB_2 targets. The microstructure, mechanical properties, and friction properties over broad ranges of temperature were detected by XRD, SEM, TEM, nano-indentation, 3D profilometer, and tribometer. It was found that the Cr-Ti-B-N films exhibited a double face-centered cubic (fcc)-CrN and amorphous-BN structure. As the Ti and B elements were introduced, the hardness and elastic modulus of Cr-Ti-B-N films increased from 21 and 246.5 GPa to a maximum value of approximately 28 and 283.6 GPa for $Cr_{38.7}Ti_{3.7}B_{6.4}N_{51.2}$ film, and then decreased slightly with a further increase of Ti and B contents. The hardness enhancement was attributed to the residual compressive stress. The friction and wear resistance of the film was improved obviously by the addition of Cr and B, as compared with the CrN film under 200 °C.

Keywords: Cr-Ti-B-N films; magnetron sputtering; microstructure; friction and wear

1. Introduction

In recent years, research in microelectronics mechanical systems, especially silicon base MEMS (Micro Electro Mechanical Systems), has been faced with reliability and service life problems. This is as a result of friction between surfaces such as the shafts, sleeves, pipes, gears, and the micro motor, which is in relative motion and also wears of parts under light load.

Nanometer super-hard film provides a new and effective solution for micro mechanical abrasion problems and is likely to be used as the next generation of sliding, speaking, reading, and writing disk protective film, it can also be used for print head of thermal printer, high fax machine head, and contact sensors because of its wear resistance properties.

Since the 1980s, mechanical properties of CrN_x coatings had been studied, and Cr_2N demonstrated predominant higher hardness and CrN were provided with better oxidation resistance and lower friction coefficient [1]. Due to its excellent properties such as low friction coefficient, high corrosion resistance, wear resistance, high toughness, and low internal stress, transition metal nitrides CrN_x have been widely used as protective hard films to increase the lifetime and performance of cutting and wear proof tools today. While the main drawback of its hardness (20 GPa) [2] restrict the use of CrN. A new generation of intelligent film, which can function very well under extreme conditions, such as high speed, dry cutting, high temperature, and surface oxidation is thus needed. Therefore, the study of friction and wear behavior of thin film over broad range of ambient conditions is of great significance. It has been reported that soft phases (Ag, Cu, Au, etc.) were effective to decrease the friction coefficient over broad working temperature range. Lihua Yu et al. [3] synthesized the WCN-Ag film containing 6.6 at.% Ag has a low friction coefficient (<0.4) in the temperature range of 25–600 °C. The NbN-Ag composite films [4] reported a decreased friction coefficient from 0.65 at 0 at.% Ag to 0.35

at 19.9 at.% Ag at room temperature. Shtansky et al. [5] deposited MoCN-Ag films which maintained low friction coefficient over a wide temperature. Similarly, the role of V element working at high temperature as a result of the generation of V_2O_5 lubricating phase also has been studied extensively, such as CrV_xN [6], TiAlVN [7], TiAlN/VN [8], NbVSiN [9] etc. To further improve the properties of CrN, alloying with other element has been explored extensively [10–12]. The superhardness of TiB_2 films has been detected [13–15]. Many researchers studied the properties of Ti-Cr-B-N film [16,17]. However, there are few data on evaluating the performance of Cr based Cr-Ti-B-N thin film and no reports about the tribological properties at elevated temperature is available as of now.

In this work, the effects of the addition of Ti and B elements on the microstructure, mechanical, and tribological properties of such films were thoroughly investigated.

2. Experimental Details

Cr-Ti-B-N films with different Ti and B content were deposited on silicon wafer and AISI304 stainless steel plates (15 mm × 15 mm × 2 mm) using radio frequency reactive magnetron sputtering system with a pure Cr (99.95 at.%) and a TiB_2 compound target (99.9 at.%). Prior to films deposition, the substrates (stainless steel AISI304) were polished with sandpaper and soft cloth used to clean the surface to removed residual scratches. The polished substrate was cleaned for 15 min ultrasonically in acetone and alcohol, then sent into the sputtering chamber. The base pressure of sputtering chamber was reduced to less than 6.0×10^{-4} Pa, and the pressure during deposition was set at 3.0×10^{-1} Pa. The distance between targets and substrates was 78 mm. A two hour deposition process was carried out in the presence of an Argon gas (Ar) and Nitrogen gas (N_2) with constant Chromium target power and various TiB_2 target power. Before the sputtering of Cr-Ti-B-N films, 10 min deposition of Cr (target power, 200 W) was conducted in a pure Argon atmosphere as the transition layer to confirm a good adhesion force of the films. The samples were located on a rotating plate which ensures homogeneous and uniform films deposited on the surface of the substrates.

The phase structures were evaluated with glancing incident X-ray diffraction with a Siemens X-ray diffractometer, with Cu Kα radiation, operated at 30 kV and 40 mA. The cross-sectional morphologies and component analysis of thin films were examined with a field emission scanning electron microscopy (FE-SEM, Merlin Compact-6170, ZEISS, Jena, Germany) which was operated at 20 kV and an Energy Disperse Spectroscopy (EDS Merlin Compact-6170, ZEISS, Germany) respectively.

The microstructure was analyzed by a high resolution transmission electron microscopy (HRTEM, JEOL, JEM-2100F, Tokyo, Japan) operated at 200 kV. The nanoindentation hardness and elastic modulus were all investigated by means of nanoindenter ($CPX + NHT^2 + MST$), equipped with a diamond Berkovich indenter tip (3-side pyramid). An automatic indentation mode was programmed to place indentations with a 3 × 3 array, averaging data on the hardness of the film. The maximum load of 3 mN was used to meet the criterion of $d/h < 0.1$, averting the influence of the substrate during the hardness test, where d is the indenter penetration depth into the film, h is the film thickness. The ball-on-disc dry wear test was conducted on the stainless steel substrates at ambient conditions by using a UTM-2 CETR tribometer with an alumina ball as counterpart (diameter, 9.38 mm). The normal load, sliding speed, sliding time, and radius of wear track during the tests were 3 N, 50 r/min, 30 min and 4 mm, respectively. The wear tracks morphologies were examined with a 3D profilometer (Bruker DEKTAK-XT, Billerica, MA, USA) and wear rate (W_s) of the films were calculated using Equation (1).

$$W_s = \frac{C \times S}{F \times L} \tag{1}$$

where C is the perimeter of the wear crack (mm), S is the wear crack area (mm^2), F is the normal load (N) and L is the sliding length. The residual stress of the film was determined by means of the Stoney's formula (Equation (2)).

$$\sigma = \frac{E_s T_s^2 \left(\frac{1}{R_s} - \frac{1}{R_f} \right)}{6(1 - v_s) T_f} \tag{2}$$

where E_s is Young's modulus, T_s is thickness of substrate, R_s is curvature radius of substrate, ν_s is Poisson's ratio of silicon substrate, R_f is curvature radius of film, and T_f is thickness of the film. The curvature radii were also examined by the Bruker 3D Profiler.

3. Results and Discussion

3.1. Elemental Compositions and Microstructure of Cr-Ti-B-N Film

Table 1 shows the elemental compositions and film thickness of Cr-Ti-B-N films with various the powers of TiB_2 composite target. As shown in Table 1, with the increase of the power of TiB_2 composite target, the Cr content in the films gradually decreases, with a corresponding increase of B and Ti content. In addition, the film thickness of the films increases with the increase of the power of TiB_2 composite target.

Table 1. Elemental compositions and film thickness of Cr-Ti-B-N films with various the powers of TiB_2 composite target.

TiB_2 Target Power (W)	Cr (at.%)	Ti (at.%)	B (at.%)	N (at.%)	Thickness of Film (μm)
0	53.7 ± 2.7	0	0	46.3 ± 2.4	1.1 ± 0.1
80	48.6 ± 2.4	1.7 ± 0.1	2.4 ± 0.1	47.3 ± 2.4	1.2 ± 0.1
100	43.9 ± 2.2	2.4 ± 0.1	4.0 ± 0.2	49.7 ± 2.5	1.2 ± 0.1
120	38.7 ± 1.9	3.7 ± 0.2	6.4 ± 0.3	51.2 ± 2.6	1.3 ± 0.1
140	33.4 ± 1.7	5.3 ± 0.3	7.6 ± 0.4	53.7 ± 2.7	1.4 ± 0.1

Figure 1 shows the X-ray diffraction patterns of Cr-Ti-B-N films with various Ti and B contents. As shown in Figure 1, for the binary CrN film, three diffraction peaks at ~36°, ~44° and ~78° are detected, which are corresponding to the face-centered cubic (fcc) CrN (111), Cr interlayer and fcc-CrN (311) repectively, based on the ICCD card 11-0065. For each pattern of quaternary Cr-Ti-B-N films, the diffraction peaks of the films are similar to that of the binary CrN film, and no other diffraction peaks corresponding to the crystalline phases such as TiB_2 and CrB_2 are not observed. Besides this, the diffraction peaks of Cr-Ti-B-N films gradually shift to higher angle, this suggests that the combination of Ti and B elements into the Cr-Ti-B-N films leads to the decrease of the lattice constant. The grain size of the films was calculated by the Scherrer's equation and the results show that the grain size of the films decreases gradually from about 33 nm for binary CrN film to 15 nm for quaternary $Cr_{33.4}Ti_{5.3}B_{7.6}N_{53.7}$ film.
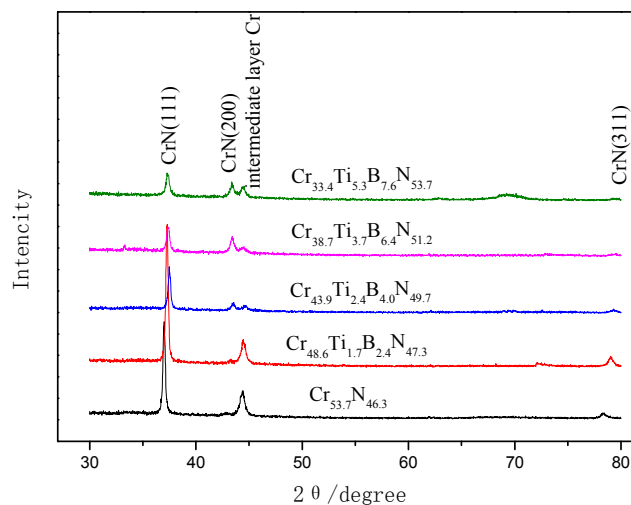
Figure 1. X-ray diffraction patterns of Cr-Ti-B-N films.

Figure 2 illustrates the cross-sectional SEM images of Cr-Ti-B-N films with various Ti and B contents. As illustrated in the Figure 2a, the binary CrN film exhibits a columnar-growth and dense structure. As the increase of the Ti and B contents in the films, as shown in Figure 2b, the columnar-growth and dense structure disappears and the $Cr_{33.4}Ti_{5.3}B_{7.6}N_{53.7}$ film shows an isometric structure.

(a)   (b)
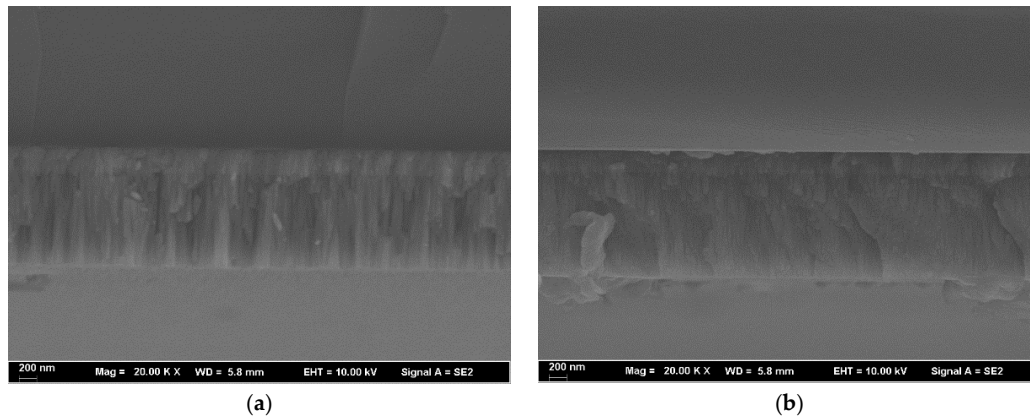
Figure 2. The cross-sectional SEM images of Cr-Ti-B-N films with various Ti and B contents: (**a**) CrN; (**b**) $Cr_{33.4}Ti_{5.3}B_{7.6}N_{53.7}$.

In order to further analyze the microstructure of Cr-Ti-B-N films, the microstructure of $Cr_{43.9}Ti_{2.4}B_{4.0}N_{49.7}$ film is investigated by high-resolution transmission electron microscope (HRTEM) and the results is shown in Figure 3. As shown in Figure 3, the $Cr_{43.9}Ti_{2.4}B_{4.0}N_{49.7}$ film exhibits a nano-composite microstructure and is consisted of nanocrystallites and amorphous phase. Besides this, three different lattice fringes with the lattice spacing of ~0.240 nm, ~0.204 nm, and ~0.156 nm are detected. Those lattice fringes are corresponding to the fcc-CrN (111), (200), and (220), since the values of lattice spacing of fcc-CrN (111), (200), and (220) (ICCD card 11-0065) are 0.2394 nm, 0.2068 nm, 0.1463 nm, and 0.1249 nm, respectively. The corresponding selected area electron diffraction (SEAD) pattern of $Cr_{43.9}Ti_{2.4}B_{4.0}N_{49.7}$ film is also shown in Figure 3 as an inset. The diffraction rings can be referred to as the lattice planes of fcc-CrN (111), (200), (220), and (311). These results are in agreement with the XRD pattern. Similar studies [18] also reported the existence of BN amorphous phase.
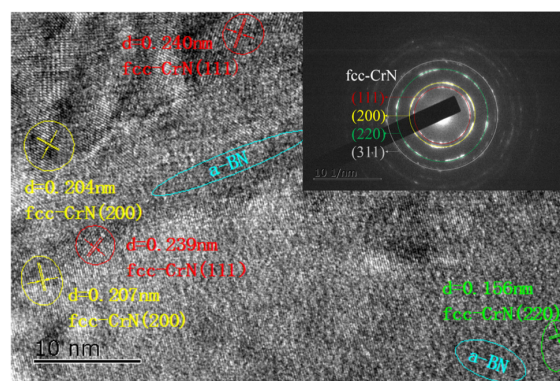
Figure 3. HRTEM micrograph and SAED pattern of $Cr_{43.9}Ti_{2.4}B_{4.0}N_{49.7}$ film.

3.2. Mechanical Properties

Figure 4 shows the hardness and elastic modulus of Cr-Ti-B-N films with the increasing Ti and B contents. As the Ti and B elements were introduced, the hardness and elastic modulus of Cr-Ti-B-N films increased from 21 and 246.5 GPa to a maximum value of approximately 28 and 283.6 GPa for $Cr_{38.7}Ti_{3.7}B_{6.4}N_{51.2}$ film, and then decreased slightly with further increase of Ti and B contents.
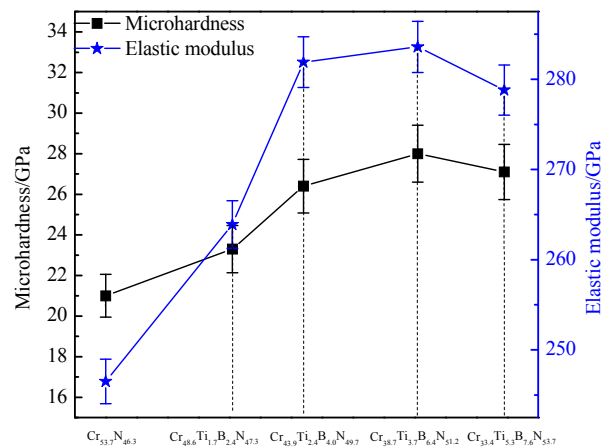
Figure 4. Hardness and elastic modulus of Cr-Ti-B-N films.

The hardness enhancement might be attributed to the solution of Ti into the films due to the different of radius of Ti, Cr atoms. The radius Cr and Ti is 0.125 nm and 0.146 nm, respectively, with the replacement of Ti into the CrN film, a strong lattice distortion will emerge, thus generate large distortion energy. On the other way, CrN and TiN have the same crystal structure with a face-centered cubic lattice type of NaCl. According to the laws of Hume-Rothery, the smaller radius anion (N) occupied face-centered cubic lattice, while Cr and Ti cations were forced into the pores of octahedral; together with the similar crystal lattice parameters between CrN and TiN, it's easy to form a continuous supersaturated solid solution. It can be concluded that the solid solution strengthening, the refined crystalline strengthening, and the increase of residual compressive stress all played a role in enhancing the hardness of the film [19]. While the reduction in hardness with a further increase in Ti and B contents after maximum hardness is as a result of increase of amorphous BN phase [20–22].

Musil [23] and Leyland [24] suggested that the fracture toughness of nanocrystalline films would be improved by high ratios of H/E (resistance against elastic strain to failure) and H^3/E^{*2} (resistance against plastic deformation). By examining the H/E and H^3/E^{*2} values of the films, as shown in Figure 5, it can be seen that Cr-Ti-B-N films exhibit improved H^3/E^{*2} values of between 0.16 and 0.22 GPa, as compared to a low value of 0.13 GPa of CrN film. The variation tendency of the values with H/E and H^3/E^{*2} are corresponding to the variation of the hardness. The highest H/E value of 0.098 was found in $Cr_{38.7}Ti_{3.7}B_{6.4}N_{51.2}$ films, suggesting this film may exhibit better toughness and wear resistance as compared to the other films.
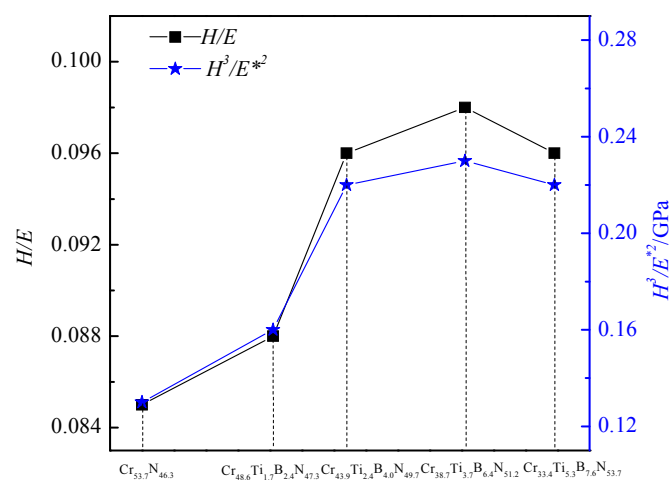
Figure 5. Calculated H/E and H^3/E^{*2} values of Cr-Ti-B-N films.

Figure 6a shows the load-displacement curves of $Cr_{38.7}Ti_{3.7}B_{6.4}N_{51.2}$ film (3.7 at.% Ti) obtained from the nanoindentation measurement. The amounts of Plastic deformation and Elastic deformation are shown clearly. Figure 6b shows amount of Plastic deformation and Elastic deformation of Cr-Ti-B-N films with various Ti and B contents. We can conclude that with an increasing of the Ti and B contents, the plastic deformation depths are 50, 41.3, 38.5, 33.6, 36 nm; the elastic deformation displacements are 46.3, 47.6, 48, 49.6, 48.4 nm, respectively which are corresponding to the results of examined H/E and H^3/E^{*2} values. The indentation depth decreased with an increasing of the Ti and B contents whiles the hardness increases with an increase of the Ti and B contents.

(**a**)

(**b**)
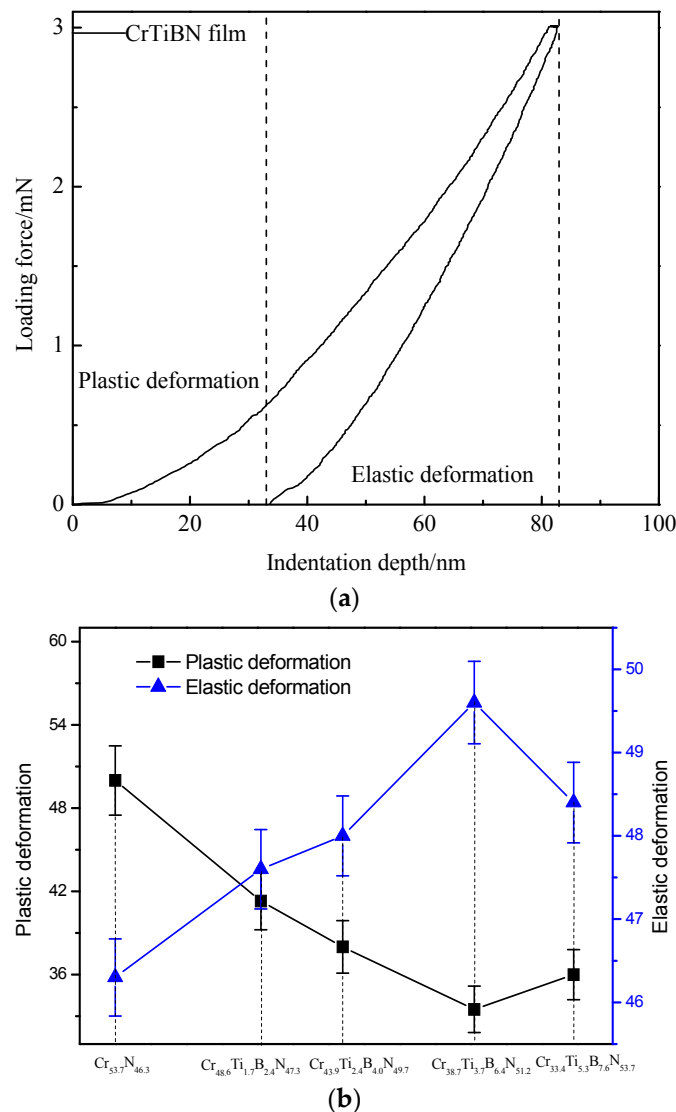
Figure 6. (**a**) Curves of nanoindention of $Cr_{38.7}Ti_{3.7}B_{6.4}N_{51.2}$ film; (**b**) amount of Plastic deformation and Elastic deformation of Cr-Ti-B-N films.

3.3. Tribological Performance at Room Temperature

The ball-on-disk wear test was conducted to evaluate the tribological properties of the films. The wear tests on the film with various Ti and B contents using an Alumina (Al_2O_3) ball was performed. As shown in Figure 7, the wear rate and friction coefficient decreased with an increase in Ti and B contents from $Cr_{53.7}N_{46.3}$ film to $Cr_{33.4}Ti_{5.3}B_{7.6}N_{53.7}$ film and a further increases in Ti and B contents resulted in increase in both wear rate and friction coefficient. Hence the optimal parameter was obtained at a Titanium content of 3.7 at.%, which is in complete agreement with the suggestion that

higher wear resistance is achieved with better H/E and H^3/E^{*2} values. The addition of Ti and B marginally decreased the friction coefficient at room temperature.
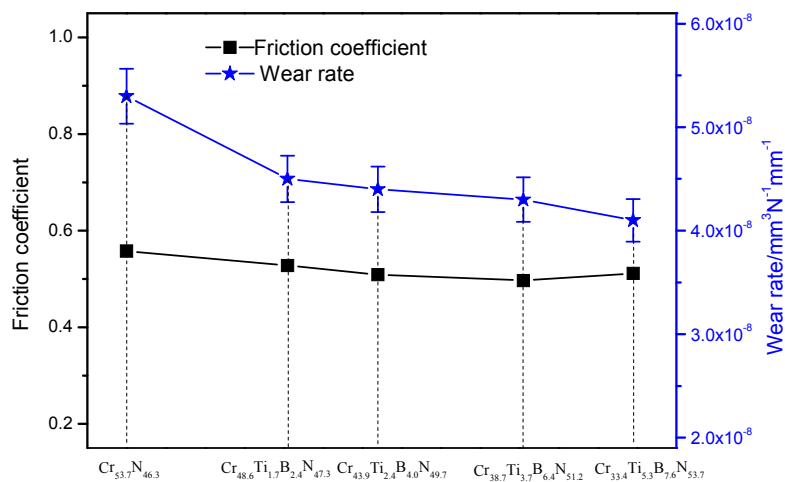
Figure 7. Friction coefficient and wear rate of Cr-Ti-B-N films at room temperature.

The wear track morphologies of Cr-Ti-B-N films with different Ti and B contents are shown in Figure 8. The confined and superficial wear track corresponded with the uppermost hardness and a better H/E value when the Ti content reached 3.7%. From Figure 8 we can conclude that the main wear patterns of Cr-Ti-B-N film with different Ti and B contents was abrasive wear, and the wear debris were accumulated at the edge of the wear track. In general, the film showed excellent wear resistance.
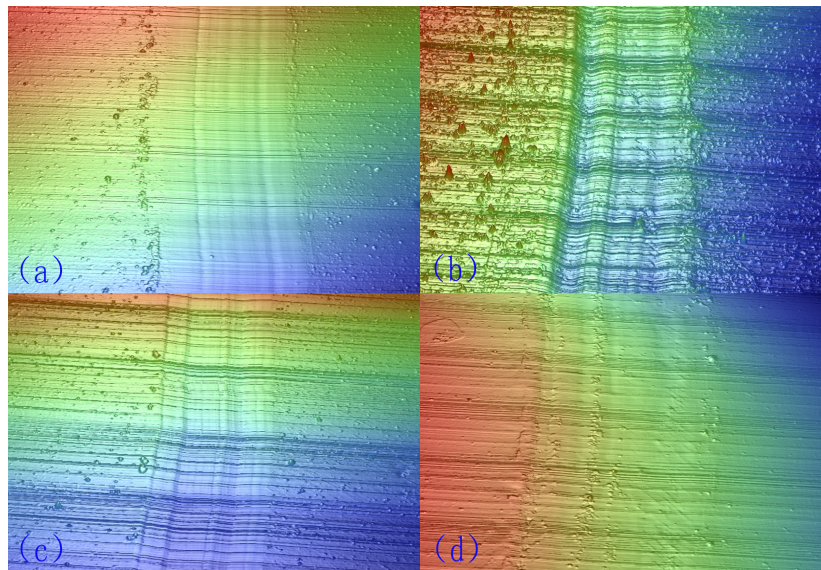
Figure 8. 3D wear track morphologies of Cr-Ti-B-N films: (**a**) $Cr_{48.6}Ti_{1.7}B_{2.4}N_{47.3}$; (**b**) $Cr_{43.9}Ti_{2.4}B_{4.0}N_{49.7}$; (**c**) $Cr_{38.7}Ti_{3.7}B_{6.4}N_{51.2}$ and (**d**) $Cr_{33.4}Ti_{5.3}B_{7.6}N_{53.7}$.

3.4. Tribological Performance at Elevated Temperature

Plots of friction coefficient about CrN film and $Cr_{38.7}Ti_{3.7}B_{6.4}N_{51.2}$ composite film at different temperature are shown in Figure 9. The friction coefficient of both films decreased continually and then tended to a stable value while the value tested at 800 °C showed a decline. The minimum friction coefficient of CrN film was 0.32 obtained at 400 °C while the CrTiBN composite film was 0.38 acquired at 800 °C. As shown in Figure 9, the addition of Ti and B elements significantly improved the

friction resistance under 200 °C. This attributed to the production of boron oxide which with lower shear modulus. With the elevated temperature higher than 400 °C, the boron oxide will melt and volatilization gradually and lots of defects generated at grain boundary, resulting in the rise of friction coefficient [25].
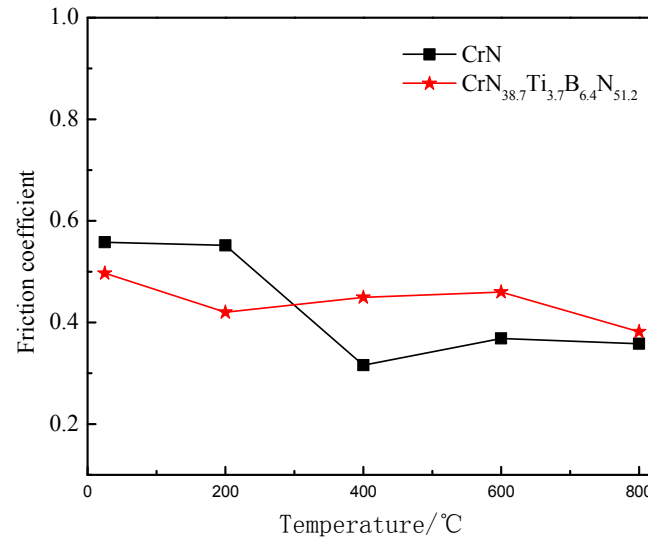
Figure 9. Friction coefficient of CrN film and $Cr_{38.7}Ti_{3.7}B_{6.4}N_{51.2}$ composite film at different temperature.

Figure 10 shows the wear rate of CrN film and $Cr_{38.7}Ti_{3.7}B_{6.4}N_{51.2}$ composite film at different temperatures. It can be observed that the wear rate increases with an increase in temperature. With the lifted temperature, the wear rate increased gradually which, due to the reduction of hardness and oxidation. The wear rate of CrN film tested at 200 °C rose sharply because of the wear out of the film. The wear resistance of $Cr_{38.7}Ti_{3.7}B_{6.4}N_{51.2}$ film was enhanced obviously under 400 °C.
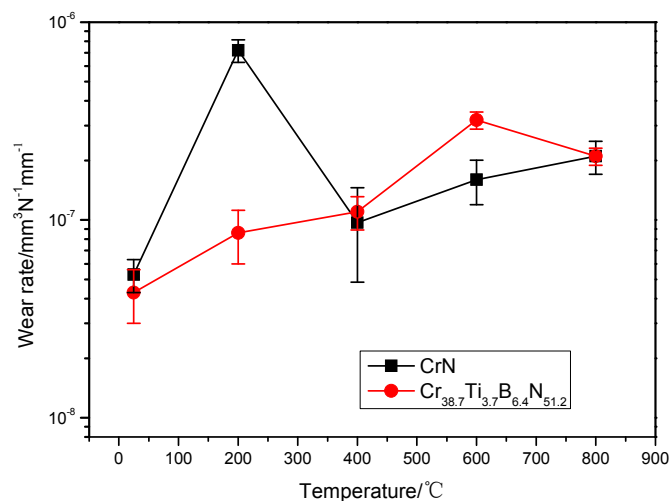
Figure 10. Wear rate of CrN film and $Cr_{38.7}Ti_{3.7}B_{6.4}N_{51.2}$ composite film at different temperature.

Figure 11 shows the friction coefficient of CrN film and $Cr_{38.7}Ti_{3.7}B_{6.4}N_{51.2}$ composite film as a function of wear duration at 200 °C in sliding against Al_2O_3 ball. The CrN film was worn out in 10 min while the $Cr_{38.7}Ti_{3.7}B_{6.4}N_{51.2}$ composite film was worn out after 20 min, which indicated an obvious improvement of the friction and wear resistance ability at 200 °C. The wear out of CrN film leads to a relative high value of the results, which are in good agreement of Figures 9 and 10.
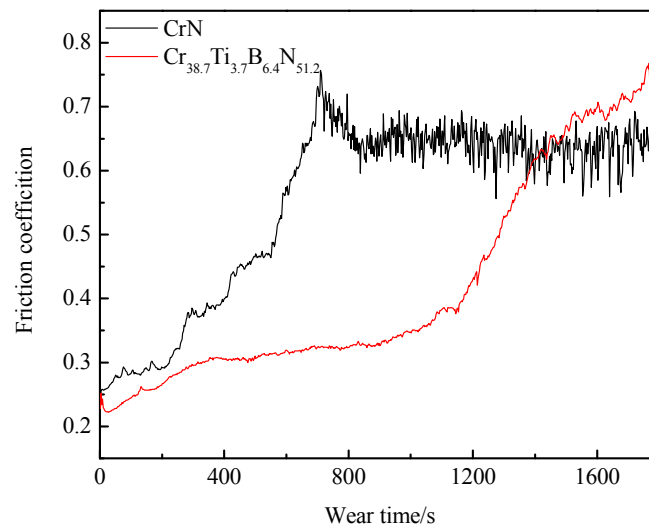
Figure 11. Friction curves of CrN film and $Cr_{38.7}Ti_{3.7}B_{6.4}N_{51.2}$ composite film tested at 200 °C.

To further confirm the changes in wear rate at different temperatures, the XRD pattern of $Cr_{38.7}Ti_{3.7}B_{6.4}N_{51.2}$ film at different temperature are shown in Figure 12. The slight increase in coefficient of friction and wear rate values are attributed to low hardness, the grains growth and the broader cracks at elevated temperature. While the sudden decrease in values at 800 °C may be as a result of the generation of mass lubricants of oxides such as TiO_2, Cr_2O_3 [20,26]. Several oxide peaks of Ti and Cr were detected only at 800 °C which confirms the appearance of oxide lubricants. Pilling and Bedworth first put forward the integrity of the oxide film. The ratio of volume fraction of metal oxide compared to metal is as a judgment of oxide film intactness, namely the PBR (Pilling Bedworth Ratio). Practice has proved that good protective oxide film of PBR value should be 1 < PBR < 2.5. The PBR values of TiO_2 and Cr_2O_3 were 1.95 and 1.99, respectively. In other words, the temperature of the grinding crack area is higher than the actual set temperature, and then the phase change of materials [27,28] caused by the high temperature and the flash temperature of friction made the wear aggravation.
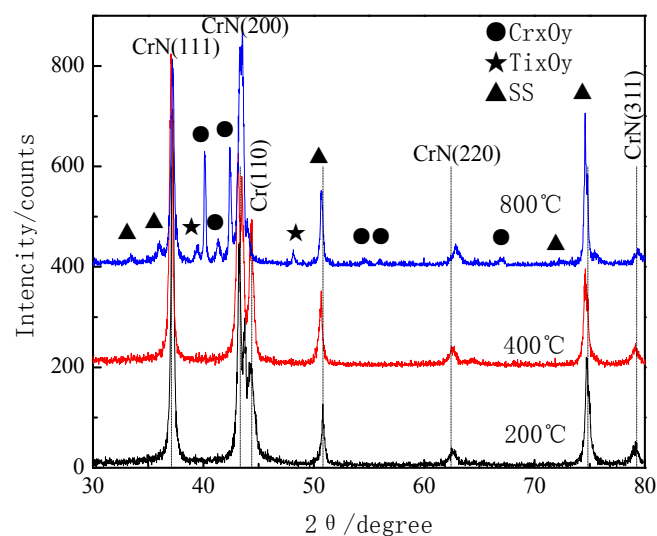
Figure 12. XRD patterns of $Cr_{38.7}Ti_{3.7}B_{6.4}N_{51.2}$ composite film after wear test at different temperature.

Figure 13 shows the changes of atomic fraction of Oxygen (O) of $Cr_{38.7}Ti_{3.7}B_{6.4}N_{51.2}$ film after wear test at different temperature. EDS results show increase in Oxygen content as a function of

temperature. Compared with the film out of the grinding crack zone, the oxygen content within the trajectory was significantly increased. This is mainly because friction makes the contact surface temperature higher and then oxidation reactions are more likely to proceed.
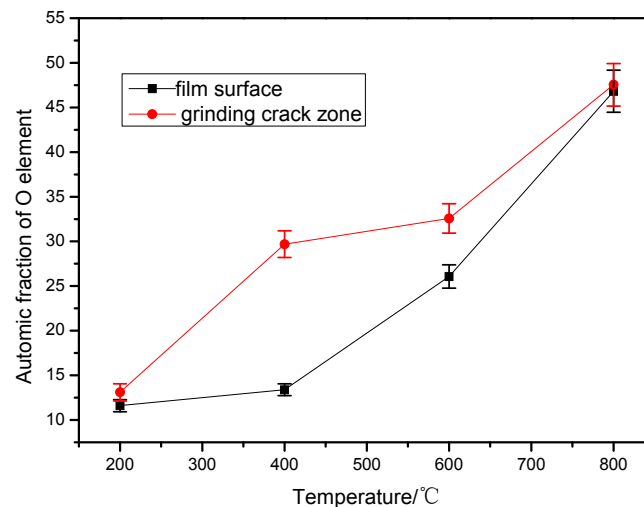
Figure 13. Atomic fraction of O element of the $Cr_{38.7}Ti_{3.7}B_{6.4}N_{51.2}$ film after wear test at different temperature.

The SEM morphologies of wear track of $Cr_{38.7}Ti_{3.7}B_{6.4}N_{51.2}$ film at elevated temperatures are shown in Figure 14. The wear track morphologies at different temperature reveal diverse worn out mechanisms such as abrasive wear, adhesive wear, plastic deformation, and crack etc. The wear track of $Cr_{38.7}Ti_{3.7}B_{6.4}N_{51.2}$ film tested at 800 °C exhibited obvious micro-cracks. Surface micro-cracks may have an effect of storing lubricants and collecting the wear debris produced in the process of wear testing. The hard grinding grain was collected within the micro cracks, reducing the damage for lubricating film. As a result, the friction coefficient and wear rate decreased evidently and thus prolong the life of the film.
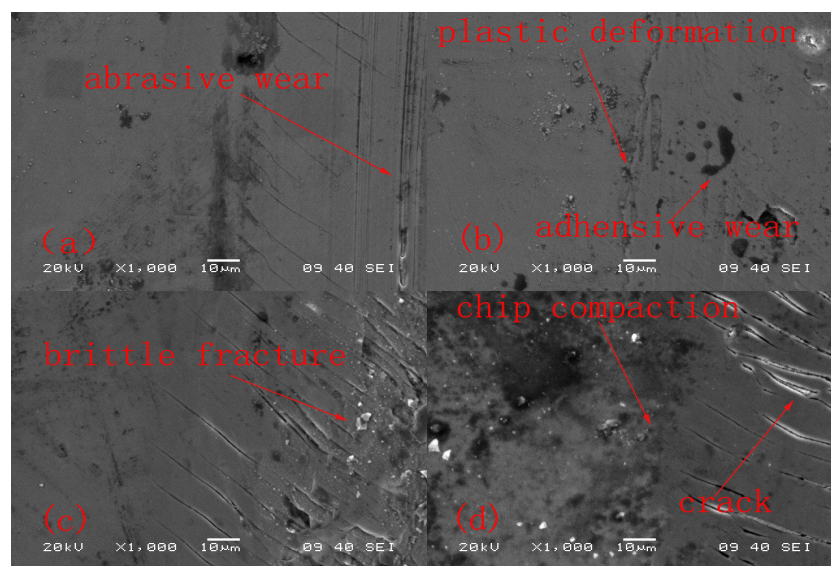
Figure 14. Wear morphology of $Cr_{38.7}Ti_{3.7}B_{6.4}N_{51.2}$ film at elevated temperature characterized by SEM: (**a**) 200 °C; (**b**) 400 °C; (**c**) 600 °C and (**d**) 800 °C.

With the oxidation of materials at different temperatures, there were changes in surface morphology and color of the films; this is due to the diverse morphologies of the film under different temperature and the generation of new oxides, respectively. After the wear test, the color of Cr-Ti-B-N film changed from silver to purple at the temperature of 600 °C; however, the uncoated samples color changed to gold at 400 °C. This indicated a higher oxidation resistance of the Cr-Ti-B-N film.

4. Conclusions

Several films of Cr-Ti-B-N with a pure Cr target at a constant radio frequency power of 200 W and a series of TiB$_2$ compound targets were fabricated using the reactive magnetron sputtering system. The microstructure, mechanical, and tribological properties of the film was strongly influenced by the TiB$_2$ target power. The cross-sectional morphology showed that the growth mechanism changed from the columnar crystal to isometric crystal with the addition of Titanium and Boron to CrN film. The Cr-Ti-B-N films exhibited a double face-centered cubic (fcc)-CrN and amorphous-BN structure. As the Ti and B elements were introduced, the hardness and elastic modulus of Cr-Ti-B-N films increased from 21 and 246.5 GPa to a maximum value of approximately 28 and 283.6 GPa for Cr$_{38.7}$Ti$_{3.7}$B$_{6.4}$N$_{51.2}$ film, and then decreased slightly with further increase of Ti and B contents. The hardness enhancement was attributed to the residual compressive stress. The friction and wear resistance of the film was improved obviously by the addition of Cr and B as compared with the CrN film under 200 °C. It can be conclude that the Cr$_{38.7}$Ti$_{3.7}$B$_{6.4}$N$_{51.2}$ film exhibited improved hardness and wear resistance over broad ranges of ambient conditions.

Author Contributions: Lihua Yu conceived and designed the experiments; Lihua Yu and Huang Luo performed and analyzed the data the experiments; Jianguo Bian, Hongbo Ju and Junhua Xu contributed to data analysis. Lihua Yu wrote the paper; all authors participated and discussed this work and contributed to the submitted and published manuscript.

Conflicts of Interest: The authors declare no conflict of interest.

References

1. Hones, P.; Sanjines, R.; Levy, F. Characterization of sputter-deposited chromium nitride thin films for hard coatings. *Surf. Coat. Technol.* **1997**, *94*, 398–402. [CrossRef]
2. Zeilinger, A.; Daniel, R.; Schöberl, T.; Stefenelli, M.; Sartory, B.; Keckes, J.; Mitterer, C. Resolving depth evolution of microstructure and hardness in sputtered CrN film. *Thin Solid Films* **2015**, *581*, 75–79. [CrossRef]
3. Yu, L.; Zhao, H.; Xu, J. Influence of silver content on structure, mechanical and tribological properties of WCN–Ag films. *Mater. Charact.* **2016**, *114*, 136–145. [CrossRef]
4. Ju, H.; Xu, J. Microstructure and tribological properties of NbN-Ag composite films by reactive magnetron sputtering. *Appl. Surf. Sci.* **2015**, *355*, 878–883. [CrossRef]
5. Shtansky, D.V.; Bondarev, A.V. Structure and tribological properties of MoCN-Ag coatings in the temperature range of 25–700 °C. *Appl. Surf. Sci.* **2013**, *273*, 408–414. [CrossRef]
6. Rapoport, L.; Moshkovich, A.; Perfilyev, V. High temperature friction behavior of CrV$_x$N coatings. *Surf. Coat. Technol.* **2014**, *238*, 207–215. [CrossRef]
7. Tillmann, W.; Sprute, T.; Hoffmann, F.; Chang, Y.; Tsai, C. Influence of bias voltage on residual stresses and tribological properties of TiAlVN-coatings at elevated temperatures. *Surf. Coat. Technol.* **2013**, *231*, 122–125. [CrossRef]
8. Hovsepian, P.; Lewis, D.; Luo, Q.; Münz, W. TiAlN based nanoscale multilayer coatings designed to adapt their tribological properties at elevated temperatures. *Thin Solid Films* **2005**, *485*, 160–168. [CrossRef]
9. Ju, H.; Xu, J. Influence of vanadium incorporation on the microstructure, mechanical and tribological properties of Nb–V–Si–N films deposited by reactive magnetron sputtering. *Mater. Charact.* **2015**, *107*, 411–418. [CrossRef]

10. Mallia, B.; Stüber, M.; Dearnley, P. Character and chemical-wear response of high alloy austenitic stainless steel (Ortron 90) surface engineered with magnetron sputtered Cr–B–N ternary alloy films. *Thin Solid Films* **2013**, *549*, 216–223. [CrossRef]

11. Lee, J.; Cheng, C.; Chen, H.; Ho, L.; Duh, J.; Chan, Y. The influence of boron contents on the microstructure and mechanical properties of Cr–B–N thin films. *Vacuum* **2013**, *87*, 191–194. [CrossRef]

12. Zhang, G.; Wang, L.; Yan, P.; Xue, Q. Structure and mechanical properties of Cr–B–N films deposited by reactive magnetron sputtering. *J. Alloy. Compd.* **2009**, *486*, 227–232. [CrossRef]

13. Rupa, P.K.P.; Chakraborti, P.C.; Mishra, S.K. Structure and indentation behavior of nanocomposite Ti–B–N films. *Thin Solid Films* **2014**, *564*, 160–169. [CrossRef]

14. Mayrhofer, P.H.; Mitterer, C.; Wen, J.G.; Greene, J.E.; Petrov, I. Self-organized nanocolumnar structure in superhard TiB2 thin films. *Appl. Phys. Lett.* **2005**, *86*, 131909. [CrossRef]

15. Rupa, P.K.P.; Chakraborti, P.C.; Mishra, S.K. Mechanical and deformation behaviour of titanium diboride thin films deposited by magnetron sputtering. *Thin Solid Films* **2009**, *517*, 2912–2919. [CrossRef]

16. Paternoster, C.; Fabrizi, A. Thermal evolution and mechanical properties of hard Ti–Cr–B–N and Ti–Al–Si–B–N coatings. *Surf. Coat. Technol.* **2008**, *203*, 736–740. [CrossRef]

17. Kiryukhantsev-Korneev, P.V.; Shtansky, D.V. Thermal stability and oxidation resistance of Ti–B–N, Ti–Cr–B–N, Ti–Si–B–N and Ti–Al–Si–B–N films. *Surf. Coat. Technol.* **2007**, *201*, 6143–6147. [CrossRef]

18. Ho, L.; Lee, J.; Chen, H. Structure and mechanical property evaluation of Cr–Ti–B–N films. *Thin Solid Films* **2013**, *544*, 380–385. [CrossRef]

19. Ju, H.; Yu, L.; Xu, J. Microstructure, mechanical and trobological properties of TiN-Ag films deposited by reactive magnetron sputtering. *Vacuum* **2017**, *141*, 82–88. [CrossRef]

20. Shtansky, D.V.; Sheveiko, A.N.; Petrzhik, M.I. Hard tribological Ti–B–N, Ti–Cr–B–N, Ti–Si–B–N and Ti–Al–Si–B–N coatings. *Surf. Coat. Technol.* **2005**, *200*, 208–212. [CrossRef]

21. Yu, L.; Zhao, H.; Xu, J. Mechanical, tribological and corrosion performance of WBN composite films deposited by reactive magnetron sputtering. *Appl. Surf. Sci.* **2014**, *315*, 380–386. [CrossRef]

22. Lin, J.; Moore, J.J.; Moerbe, W.C. Structure and properties of selected (Cr–Al–N, TiC–C, Cr–B–N) nanostructured tribological films. *Int. J. Refract. Met. Hard Mater.* **2010**, *28*, 2–14. [CrossRef]

23. Musil, J.; Jirout, M. Toughness of hard nanostructured ceramic thin films. *Surf. Coat. Technol.* **2007**, *201*, 5148–5152. [CrossRef]

24. Leyland, A.; Matthews, A. On the significance of the H/E ratio in wear control: A nanocomposite coating approach to optimised tribological behavior. *Wear* **2000**, *246*, 1–11. [CrossRef]

25. Erdemir, A. A crystal chemical approach to the formulation of self-lubricating nanocomposite coatings. *Surf. Coat. Technol.* **2005**, *200*, 1792–1796. [CrossRef]

26. Ju, H.; He, S.; Yu, L.; Xu, J. The improvement of oxidation resistance, mechanical and tribological properties of W2N films by doping silicon. *Surf. Coat. Technol.* **2017**, *317*, 158–165. [CrossRef]

27. Ju, H.; He, X.; Yu, L.; Xu, J. The microstructure and tribological properties at elevated temperatures of tungsten silicon nitride films. *Surf. Coat. Technol.* **2017**, *326*, 255–263. [CrossRef]

28. Ju, H.; Yu, L.; He, S.; Xu, J. The enhancement of fracture toughness and tribological properties of the titanium nitride films by doping yttrium. *Surf. Coat. Technol.* **2017**, *321*, 57–63. [CrossRef]